



# Self-polymerization of dopamine-coated zinc oxide as a potential antibacterial nanoparticle with molecular docking analysis

Yasin Albarqouni<sup>1,2</sup> · Miah Roney<sup>3,4</sup> · Kwok Feng Chong<sup>3</sup> ·  
Mohammad R. Thalji<sup>5</sup> · Gholamhassan Najafi<sup>6</sup> · Arman Abdullah<sup>1</sup>

Received: 2 September 2024 / Revised: 1 June 2025 / Accepted: 4 June 2025

© The Author(s) 2025

## Abstract

The escalating prevalence of multidrug-resistant bacteria on medical surfaces necessitates the development of innovative antibacterial strategies. In this study, we report synthesizing and evaluating zinc oxide nanoparticles functionalized with polydopamine (ZnO/PDA) as a potent antibacterial agent, exhibiting notable efficacy at a low concentration of 5 mg/mL. Structural and morphological analyses confirm the successful surface decoration of ZnO with PDA, yielding a distinctive popcorn-like architecture that facilitates bacterial growth inhibition. Antibacterial assays conducted against *Bacillus cereus* (Gram-positive) and *Escherichia coli* (Gram-negative) demonstrate superior activity against both strains, outperforming previously reported ZnO-based systems. Hemocompatibility assessments reveal excellent blood compatibility, with a hemolysis rate of only 1.13%, underscoring the nanocomposite's potential for biomedical applications. To probe molecular interactions, *in silico* docking studies are performed targeting key virulence proteins: Q81BN2\_BACCR from *B. cereus* and DHOase from *E. coli*. The ZnO/PDA nanocomposite exhibits strong binding affinities, with docking energies of  $-10.3$  kcal/mol and  $-8.4$  kcal/mol, respectively, surpassing those of clindamycin, a clinically used antibiotic. The antibacterial activity of ZnO/PDA is likely mediated through multiple mechanisms, including; direct physical disruption of the bacterial membrane by its nanostructure and molecular level interference via protein binding and generation of reactive oxygen species (ROS) by ZnO may further contribute to microbial inactivation. While this study primarily evaluates antibacterial efficacy, integrating biocompatibility, structural robustness, and scalable synthesis highlights the promise of ZnO/PDA nanocomposite for next-generation antimicrobial coatings. Future prioritizes comprehensive cytotoxicity assessments and mechanistic studies to advance clinical translation.

Extended author information available on the last page of the article

**Keywords** ZnO NPs · Polydopamine · Self-polymerization · Antibacterial activity · Multidrug resistance · Molecular docking

## Introduction

Toxigenic spore-forming bacteria, such as *Bacillus cereus* and *Clostridium* species, exhibit exceptional resistance to environmental stresses, including desiccation, radiation, chemical disinfectants, and heat [1–4]. This resilience renders conventional sanitation and pasteurization techniques ineffective for spore inactivation, posing a significant challenge to food safety and public health [5, 6]. Compounding this issue is the alarming rise of multidrug-resistant (MDR) bacterial strains, largely driven by the widespread and often indiscriminate use of antibiotics [7]. The global health threat posed by antibiotic resistance is escalating rapidly, with projections indicating that annual mortality may reach 10 million by 2050 if effective countermeasures are not implemented [8].

In response to this crisis, nanotechnology has emerged as a promising frontier for next-generation antimicrobial strategies. Engineered nanomaterials, such as silver, gold, and metal oxide nanoparticles (NPs) [9–11], have demonstrated broad-spectrum antibacterial efficacy through diverse mechanisms, including reactive oxygen species (ROS) generation, membrane disruption, and protein inactivation. Among these, zinc oxide (ZnO) NPs have garnered substantial attention due to their low cost, abundance, chemical stability, and inherent biocompatibility [12–18]. ZnO NPs have exhibited strong antimicrobial activity against a wide array of Gram-positive and Gram-negative pathogens [19–27]. Despite these advantages, the clinical and environmental deployment of ZnO remains constrained by several limitations. These include (i) Suboptimal efficacy against biofilm-forming bacteria, (ii) Variable activity across microbial species, and (iii) Cytotoxicity associated with excess release of free  $Zn^{2+}$  ions [28–30]. For instance, Habib et al. [31] demonstrated that the co-administration of ZnO NPs with conventional antibiotics significantly enhanced antibacterial activity against *Staphylococcus aureus*, with a 17 mm zone of inhibition compared to 12 mm for *E. coli*. The study also revealed synergistic reductions in the minimum inhibitory concentrations (MICs) of six antibiotics, and substantial inhibition of bacterial biofilms, rising from 34 to 37% with antibiotics alone to 65–85% when combined with ZnO NPs.

In another study, Sharma and Ghose [32] reported a dose-dependent antifungal activity of ZnO NPs against *Candida albicans*, with inhibition zones ranging from 1.5 to 11.4 mm depending on NPs concentration. Despite the promising antimicrobial efficacy of ZnO, a critical limitation lies in the cytotoxicity associated with the release of unbound  $Zn^{2+}$  ions. Thunugunta et al. [31] conducted a comparative study revealing that both ZnO NPs and free  $Zn^{2+}$  ions exert toxic effects, emphasizing the need to decouple antibacterial potency from potential biosafety risks. While  $Zn^{2+}$  ions release is central to microbial inactivation, it may simultaneously impose phytotoxic effects, particularly on meristematic plant tissues. These adverse effects are proposed to occur through multiple mechanisms, including disruption of cell wall integrity, inhibition of mitotic spindle formation, and the induction of oxidative

stress pathways [33]. Such toxicity concerns are further exacerbated by the ultra-small size (<25 nm) of ZnO NPs, which facilitates cellular uptake and enhances ion release rates [34, 35].

Recent strategies have increasingly focused on surface functionalization of ZnO NPs with organic or inorganic moieties to mitigate cytotoxicity and enhance antibacterial efficacy, particularly against biofilm-forming pathogens. Modulating particle size or tailoring surface chemistry has been shown to reduce the release of free Zn<sup>2+</sup> ion, thereby enhancing antimicrobial performance [36, 37]. In this context, surface coatings such as polydopamine (PDA) have emerged as particularly advantageous. PDA not only improves the biosafety profile of nanomaterials but also modulates ion exchange kinetics and augments antibacterial and anti-biofilm activities. These advancements represent a promising avenue to balance efficacy with biosafety in ZnO-based antimicrobial systems. PDA is a mussel-inspired, highly versatile, and biocompatible polymeric material with extensive applications in biomedicine and nanotechnology due to its insolubility, adhesion properties, and functional surface chemistry [38–45]. It exhibits controlled drug-release capabilities and intrinsic antibacterial activity, enhancing both chemical and physical bactericidal mechanisms [46]. Notably, its unique physicochemical features, including superior absorbability and anionic tunability under acidic conditions, enable effective bacterial entrapment [47]. Furthermore, it has been shown to physically interact with microbial membranes, disrupting key protein functions and promoting apoptosis, thereby amplifying its antimicrobial action [48]. These properties underscore PDA's potential as a strategic modifier for nano-systems, offering benefits such as size control, improved biocompatibility, and enhanced antibacterial and anti-fouling performance when integrated with metal oxides like ZnO [49].

In this study, ZnO NPs were synthesized via a sol–gel method and subsequently functionalized with PDA through a facile self-polymerization approach. The resulting ZnO/PDA nanocomposite was comprehensively characterized using ultraviolet–visible (UV–Vis) spectroscopy, Fourier-transformed infrared spectrometer (FT-IR), X-ray diffraction (XRD), and field-emission scanning electron microscopy (FESEM), confirming successful functionalization and retention of ZnO's crystalline framework. The antimicrobial performance of the composite was evaluated against *Bacillus cereus* and *E. coli* using both in vitro assays and in silico molecular docking studies. Minimum inhibitory concentrations (MIC) and minimum bactericidal concentrations (MBC) were determined to quantify the inhibitory and bactericidal efficiency of the ZnO/PDA nanocomposite, especially at low-dose conditions.

## Materials and methods

### Materials

Zinc acetate dihydrate (CH<sub>3</sub>COO)<sub>2</sub>Zn·2H<sub>2</sub>O, oxalic acid (H<sub>2</sub>C<sub>2</sub>O<sub>4</sub>), and ethanol were purchased from Sigma-Aldrich. Dopamine-d4 hydrochloride (C<sub>8</sub>H<sub>8</sub>D<sub>4</sub>ClNO<sub>2</sub>) was purchased from Santa Cruz Biotechnology. Mueller–Hinton Agar (MHA) was procured from Thermo Fisher Scientific.

## Synthesis of ZnO/PDA nanocomposite

ZnO NPs were synthesized via a sol–gel method as previously described [50]. Briefly, 50.1 mmol of zinc acetate dihydrate was dissolved in 300 mL of ethanol and refluxed at 60 °C under vigorous magnetic stirring for 30 min. Separately, 140 mmol of oxalic acid was dissolved in 200 mL of ethanol and gradually added dropwise to the zinc acetate solution. The resulting mixture was further refluxed at 50 °C for 60 min, then allowed to cool to room temperature. The ZnO gel was subsequently dried at 80 °C for 20 h and calcined in a flow of air (0.1 mmol/s) at 650 °C for 4 h. The PDA-functionalized ZnO nanocomposite was fabricated using a one-pot self-polymerization approach as illustrated in Fig. 1 [51]. In brief, the synthesized ZnO NPs were dispersed in a sufficient Tris–HCl buffer (pH 8.5) under mechanical stirring, followed by ultrasonication for 20 min to ensure homogeneous dispersion. Subsequently, dopamine hydrochloride (DOPA-HCl) was added, and the mixture was stirred continuously for 24 h to facilitate the self-polymerization of dopamine [52]. The resulting ZnO/PDA nanocomposite was collected by vacuum filtration, thoroughly washed with deionized water at least three times to remove unreacted residues and dried in an oven at 60 °C for 8 h. The final product was stored in a desiccator at room temperature to prevent moisture uptake.

## Structural and morphological characterizations

Successful functionalization of ZnO NPs with PDA was confirmed through a series of physicochemical characterizations. UV–Vis spectroscopy was conducted using an Agilent CARY 60 spectrophotometer to evaluate the optical absorption behavior of pure ZnO NPs and ZnO/PDA nanocomposites [53]. Changes in absorbance features provided preliminary evidence for PDA coating.



**Fig. 1** Schematic illustration of the synthesis of ZnO/PDA nanocomposite followed by its application in antibacterial assays against *Bacillus cereus* and *E. coli*

The functional groups of the fabricated ZnO NPs and ZnO/PDA nanocomposite were studied using FT-IR (Spectrum 100, PerkinElmer). Dynamic light scattering (DLS) measurements were performed using a DelsaMax Pro analyzer (SN: 3234-DMP) to determine the hydrodynamic diameter and particle size distribution. Prior to analysis, NPs suspensions were diluted in deionized water and sonicated for 10 min to achieve uniform dispersion and prevent agglomeration. The morphology features and elemental composition were analyzed via FE-SEM (JEOL, JSM7800F) equipped with energy-dispersive X-ray spectroscopy (EDS). This allowed visualization of particle shape and assessment of PDA surface coverage.

Crystallographic analysis was conducted using XRD (Rigaku Miniflex II) with Cu-K $\alpha$  radiation ( $\lambda = 1.5406 \text{ \AA}$ ) operated at 30 kV and 15 mA. Diffraction patterns were collected over a  $2\theta$  range of  $3\text{--}80^\circ$ . Any shifts in diffraction peaks, particularly those corresponding to ZnO's hexagonal wurtzite structure, were analyzed to assess the influence of PDA functionalization on crystal structure. Interlayer distances were calculated using Bragg's equation [54].

$$n\lambda = 2d\sin\theta \text{ Bragg's Equation}$$

where  $d$  is the interplanar spacing,  $\theta$  is Bragg's diffraction angle,  $n = 1$ , and  $\lambda$  is the wavelength of the X-ray used ( $1.5406 \text{ \AA}$ ).

### Hemocompatibility assessment of ZnO/PDA nanoparticles

The hemocompatibility of ZnO/PDA nanocomposite was evaluated following the guidelines of ASTM F756-17 [55], human whole blood samples were obtained from a local clinic with informed consent and subjected to triple centrifugation (3000 rpm, 15 min each) using isotonic saline solution (0.9% w/v NaCl) to isolate red blood cells (RBCs). After erythrocyte purification, 100  $\mu\text{L}$  of packed RBCs were resuspended in 900  $\mu\text{L}$  of saline containing 100  $\mu\text{g}$  of ZnO/PDA nanocomposite in sterile Eppendorf tubes ( $A_S$ ). The suspensions were incubated at  $37^\circ\text{C}$  for 3 h under static conditions to simulate physiological temperature and exposure time. Post-incubation, the samples were centrifuged at 12,000 rpm for 15 min to pellet the cells. The optical density (OD) of the supernatant, indicative of hemoglobin release, was measured at 540 nm using a UV-Vis spectrophotometer. Controls were included as follows:  $A_N$  as a negative control containing RBCs in saline and  $A_P$  as a positive control containing RBCs in distilled water. The hemolysis ratio (HR%) was calculated using the following equation, adapted from previously reported methods [2, 56].

$$\text{HR} = \frac{A_S - A_N}{A_P - A_N} \times 100(\%)$$

A hemolysis percentage below 5% is generally considered acceptable for hemocompatible materials.

## Test microorganisms

The antibacterial activity of the synthesized ZnO/PDA nanocomposite was assessed against representative Gram-positive and Gram-negative bacterial strains. Specifically, the test organisms included *E. coli* (UPMC 1480), a Gram-negative bacterium, and *Bacillus cereus* (UPMC 61), a Gram-positive bacterium. Both strains were obtained from the Universiti Putra Malaysia Culture Collection (UPMC) and were maintained under standard microbiological conditions. These strains were selected due to their clinical relevance and known resistance mechanisms, which provide a robust model for evaluating the broad-spectrum antibacterial efficacy of the ZnO/PDA nanocomposite.

## Antibacterial assay

The antibacterial activity of the synthesized nanocomposite was evaluated using agar well diffusion method to determine the zone of inhibition (ZOI). Mueller–Hinton Agar (MHA) was prepared according to standard microbiological protocols. The MHA medium was sterilized via autoclaving at 121 °C and 15 psi for 15 min, cooled to approximately 45–50 °C, and poured aseptically into sterile Petri dishes. After solidification, uniform wells (6 mm diameter) were created in the agar using a sterile cork borer [57]. Bacterial cultures were standardized to 0.5 McFarland turbidity standard, corresponding to  $\sim 5 \times 10^8$  CFU/mL, using sterile saline. Each standardized bacterial suspension (100  $\mu$ L) evenly spreads onto the surface of MHA plates using sterile cotton swabs. Nanoparticle suspensions of pure ZnO NPs and ZnO/PDA nanocomposite (5 mg/mL in sterile distilled water) were freshly prepared. A 100  $\mu$ L aliquots of each suspension was introduced into individual wells. Control wells containing only sterile distilled water were included as negative controls. The inoculated plates were incubated at  $37 \pm 0.5$  °C for 24 h under aerobic conditions. Post-incubation, the diameter of the clear zone surrounding each well was measured in millimeters using a digital caliper. Larger ZOIs indicate stronger antibacterial activity.

## Determination of MIC and MBC

The minimum inhibitory concentration (MIC) is defined as the lowest concentration of an antimicrobial agent that completely inhibits visible bacterial growth [58]. MIC determination was performed using the standard broth microdilution method. Briefly, a series of twelve twofold serial dilutions of the ZnO/PDA nanocomposite stock solution were prepared in sterile broth medium. Simultaneously, bacterial suspensions were standardized to a concentration of  $5 \times 10^6$  CFU/mL. In a sterile 96-well microtiter plate, each well received 100  $\mu$ L of the prepared bacterial inoculum and varying concentrations of ZnO/PDA nanocomposite. The plates were incubated for 24 h at  $35 \pm 2$  °C. MIC values were assessed via two methods: (1) Visual inspection of turbidity and (2) Optical density (OD) measurements at 600 nm using

a microplate reader (Tecan Infinite® M200 Pro). A well was considered inhibitory if  $OD_{600}$  was below 0.1, indicating the absence of bacterial growth. The MIC was confirmed by comparing the turbidity of the wells before and after incubation [4]. To determine the minimum bactericidal concentration (MBC), the lowest concentration that results in complete bacterial killing, aliquots of 10  $\mu$ L from each well of the MIC plate were aseptically spotted onto Mueller–Hinton Agar (MHA) plates, pre-labeled to correspond to each concentration tested. The plates were incubated under identical conditions ( $35 \pm 2$  °C for 24 h). The MBC was recorded as having the lowest concentration at which no bacterial colonies were observed on the agar surface, following established procedures [59].

## Molecular docking

Molecular docking studies were conducted to evaluate the interaction of the synthesized ZnO/PDA nanocomposite and the reference antibiotic Clindamycin with target bacterial proteins using CB-Dock, a cavity detection-guided blind docking platform [60]. The ZnO/PDA nanocomposite was structurally modeled using the ChemSketch program and saved in.mol format. Two target proteins were selected for this study: (i) Q81BN2\_BACCR, a master regulator of peptidoglycan biosynthesis in *Bacillus cereus* [61], and (ii) Dihydroorotase (DHOase) from *E. coli*, a key enzyme in the de novo pyrimidine biosynthesis pathway [62]. The crystal structures of these proteins were retrieved from the Protein Data Bank (PDB IDs: 3B55 and 2EG7, respectively), with resolutions below 3 Å. CB-Dock automatically identified potential binding cavities and calculated the docking box dimensions by analyzing the spatial characteristics of both the ligand and receptor. Docking was carried out using AutoDock Vina 1.1.2 [63], where the receptor was input as a.pdb file and the ligand as a.mol file. The software performed docking at several top-ranked cavities based on predicted binding affinity and cavity volume. The docking pose with the highest binding affinity (lowest binding energy) and the largest cavity volume was considered the most favorable binding site for each ligand. Binding conformations were visualized and further analyzed to understand key interaction residues and binding modes, facilitating insights into the molecular basis of antimicrobial activity.

## Results and discussion

### Structural and morphological characterizations

The as-synthesized ZnO precursor initially formed a white hydrous gel (Fig. 1), which upon calcination at 650 °C for 4 h, underwent complete dehydration and crystallization to yield a fine white powder. The optical absorption properties of ZnO and ZnO/PDA composite are presented in Fig. 2a. Pristine ZnO exhibited a strong absorption band near 370 nm [64], characteristic of its wide bandgap and indicative of spherical nanostructures exhibiting quantum confinement effects [65–67]. Upon functionalization with polydopamine (PDA), significant changes

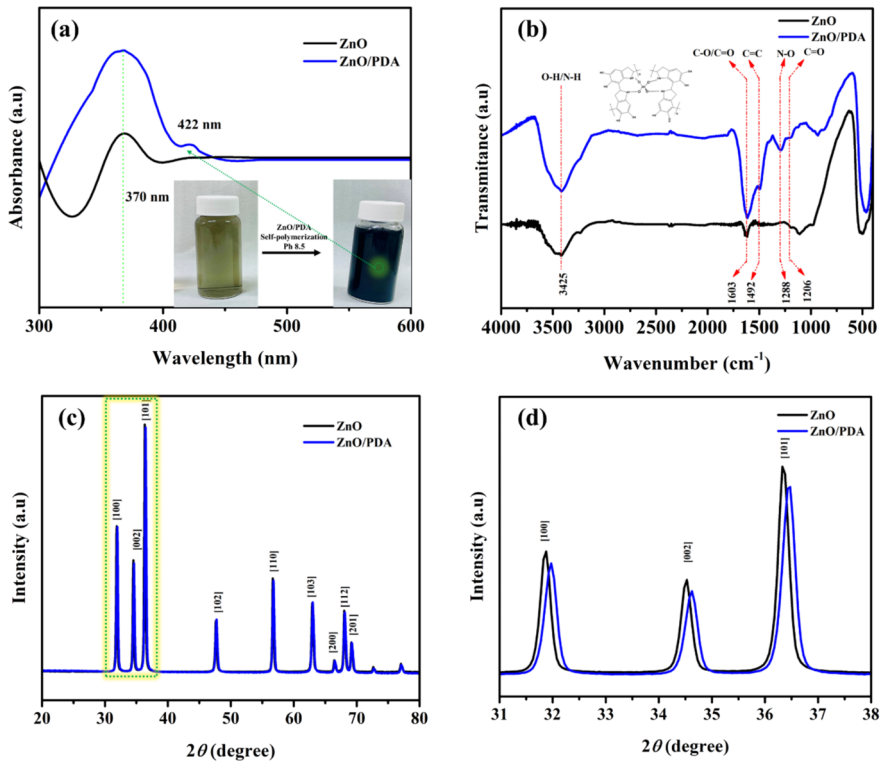


**Fig. 2** **a** UV–Vis absorption spectra, **b** FT-IR spectra, **c** XRD patterns, and **d** magnified XRD inset highlighting peak shifts of ZnO NPs and the ZnO/PDA nanocomposite

in the absorption spectrum were observed. The ZnO/PDA composite displayed a distinct redshift, with a new absorption maximum emerging at 422 nm, alongside a broadening of the original ZnO peak. This behavior can be ascribed to interfacial charge transfer processes between ZnO and PDA, as well as the intrinsic visible light absorption of PDA attributed to its  $\pi$ -conjugated aromatic system [68]. The peak broadening further suggests the formation of interfacial states or charge-transfer complexes, consistent with prior reports on hybrid organic–inorganic nanomaterials [69, 70].

FT-IR spectroscopy was employed to confirm the surface functionalization and assess the chemical bonding environment of the ZnO/PDA composite, as illustrated in Fig. 2b. Both ZnO and ZnO/PDA nanocomposite samples exhibit characteristic Zn–O stretching vibrations in the 480–500 cm<sup>-1</sup> range. A redshift in the Zn–OH stretching vibration, appearing between 795 and 882 cm<sup>-1</sup>, was observed in the ZnO/PDA sample, indicating alterations in surface hydroxyl groups upon PDA attachment [71]. Additional peaks in the composite spectrum at 1288 cm<sup>-1</sup>, 1338 cm<sup>-1</sup>, 1492 cm<sup>-1</sup>, and 1603 cm<sup>-1</sup> correspond to C=O/C–O, N–O, C=C, and C=N stretching vibration, respectively, clear signatures of the successful PDA

incorporation. Furthermore, a broadened absorption band centered at  $3425\text{ cm}^{-1}$ , attributable to N–H and O–H stretching modes, confirms the presence of hydroxyl and amine functionalities from the PDA [72].

XRD analysis was conducted to examine the crystalline phase and assess structural modifications induced by PDA functionalization (Fig. 2c). Both ZnO NPs and ZnO/PDA nanocomposites exhibited diffraction patterns consistent with the hexagonal wurtzite structure of ZnO (JCPDS No. 36-1451), confirming that PDA incorporation does not alter the primary crystal phase. However, subtle yet reproducible shifts in diffraction peaks toward higher  $2\theta$  angles were observed in ZnO/PDA sample, as presented in Fig. 2d, accompanied by a noticeable reduction in peak intensity and slight broadening. These features indicate increased micro-strain and partial loss of long-range crystallinity, likely due to the formation of interfacial bonds between PDA and ZnO. The  $\pi$ -conjugated structure of PDA, enriched with catechol and amine functional groups, may interact with  $\text{Zn}^{2+}$  surface sites, thereby perturbing the local lattice environment. A comparative analysis of the lattice parameters, summarized in Table 1, reveals an overall expansion in lattice size across several crystallographic planes upon PDA incorporation [73, 74]. Interestingly, Bragg’s law calculations show a decrease in interplanar spacing ( $d$ -spacing) for certain planes, despite the increase in unit cell volume, suggesting anisotropic lattice distortions. These structural perturbations confirm the successful surface modification of ZnO by PDA and highlight its influence on crystallinity and lattice strain.

The surface morphologies of the synthesized ZnO and ZnO/PDA nanocomposite were scrutinized by FE-SEM analysis at varying magnification levels (Fig. 3). The images reveal notable morphological differences between the pristine and functionalized samples. Pristine ZnO nanoparticles exhibited uniform spherical shapes with particle sizes ranging from 84 to 106 nm. Upon functionalization with polydopamine (PDA), a distinct increase in particle diameter is observed, reaching approximately 210 nm on average. The modified structures adopt a popcorn-like morphology, indicative of successful surface coating. This significant increase in particle

**Table 1** Comparison of XRD data for ZnO NPs and ZnO/PDA nanocomposite

No	ZnO NPs			ZnO/PDA nanocomposite		
	( $2\theta$ )	$d$ -spacing (Å)	Crystallite Size (Å)	( $2\theta$ )	$d$ -spacing (Å)	Crystallite size (Å)
1	31.84	2.81	1960	31.93	2.80	2267
2	34.49	2.60	1683	34.58	2.59	2227
3	36.32	2.47	1227	36.41	2.47	1227
4	47.61	1.91	696	47.69	1.91	585
5	56.66	1.62	1162	56.73	1.62	1087
6	62.92	1.48	562	62.98	1.47	570
7	66.44	1.41	514	66.50	1.40	613
8	68.01	1.38	852	68.07	1.38	872
9	69.15	1.36	673	69.21	1.36	760

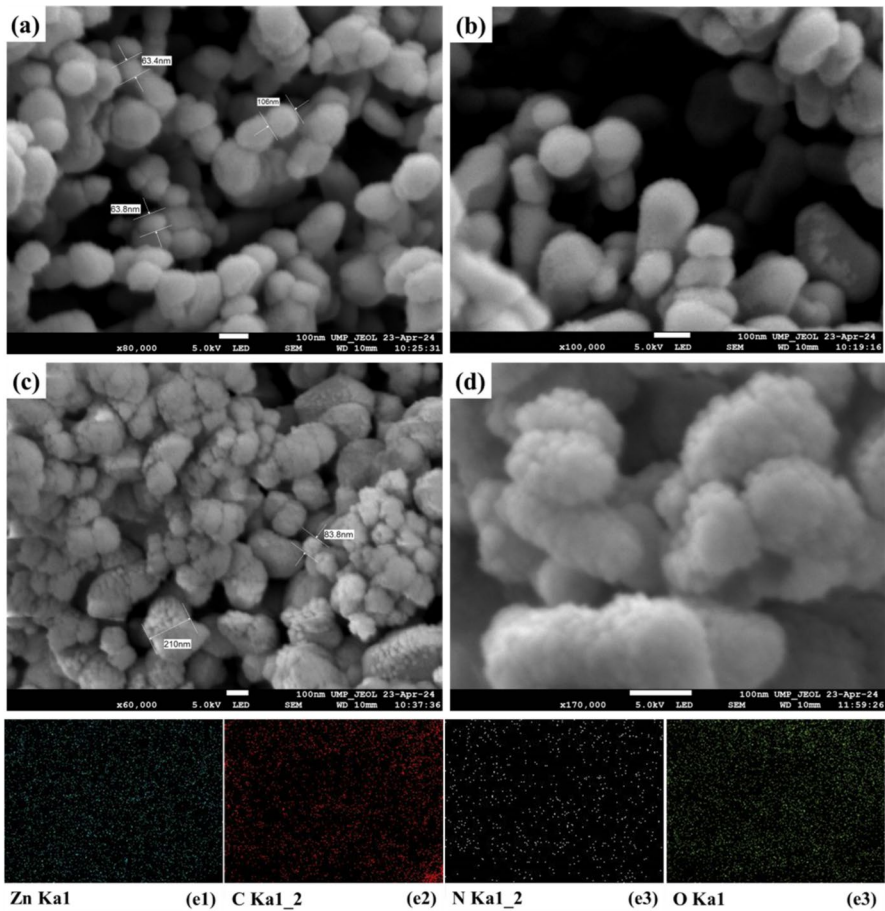


**Fig. 3** FE-SEM images of **a–b** ZnO NPs and **c–d** ZnO/PDA nanocomposite at different magnifications. **e** EDS analysis of the ZnO/PDA nanocomposite

size provides strong morphological evidence for the deposition of a PDA shell onto the ZnO cores. Energy-dispersive X-ray spectroscopy (EDS) and elemental mapping were performed to further validate the composition and surface modification of the ZnO/PDA nanocomposite. The elemental distribution maps confirmed a homogeneous dispersion of carbon, nitrogen, oxygen, and zinc across the nanocomposite

**Table 2** EDS atomic and weight ratios of the ZnO NPs and ZnO/PDA nanocomposite

No	ZnO NPs		ZnO/PDA nanocomposite			
	Zinc (Zn)	Oxygen (O)	Zinc (Zn)	Oxygen (O)	Carbon (C)	Nitrogen (N)
Weight (%)	83.16	16.84	43.23	23.50	28.98	4.29
Atomic (%)	54.71	45.29	13.64	30.29	49.76	6.31

surface. Quantitative EDS analysis, summarized in Table 2, shows increased carbon and nitrogen content in the ZnO/PDA composite compared to pristine ZnO. These findings are consistent with the incorporation of PDA, whose molecular structure is rich in carbon and nitrogen, thereby substantiating the successful functionalization of ZnO with polydopamine [72].

Dynamic light scattering (DLS) measurements further corroborated the morphological changes induced by polydopamine (PDA) functionalization. The hydrodynamic diameter of pristine ZnO nanoparticles was determined to be 1801.6 nm, which markedly increased to 2722.4 nm upon PDA coating. This substantial enlargement reflects the formation of a PDA shell and is consistent with the known behavior of DLS measurements, which typically yield larger particle sizes than dry-state imaging techniques such as transmission electron microscopy (TEM) and FE-SEM. This discrepancy arises due to the contribution of the solvation shell and interfacial interactions between the nanoparticles and the surrounding medium in suspension [75].

Regularization analysis of the DLS data (Fig. 4b) revealed a monomodal particle size distribution with a polydispersity index (PDI) of 35.9%, indicating moderate heterogeneity within the ZnO/PDA nanocomposite dispersion. Notably, the inferred spherical morphology from DLS measurements is particularly advantageous for biomaterial applications, as spherical particles offer a high surface-to-volume ratio while reducing edge-induced mechanical stress on cellular membranes. The colloidal stability of the suspension was further supported by the intensity autocorrelation function (Fig. 4a), which exhibited a consistent exponential decay profile characteristic of Brownian motion, with no evidence of aggregation artifacts or sedimentation effects [76, 77].

## Hemocompatibility Results

The hemolysis assay demonstrated that the ZnO/PDA nanocomposite exhibited excellent hemocompatibility, with a measured hemolysis rate of just 1.13%, well below the internationally accepted threshold of 5% for biomaterial safety. As shown in Fig. 4, this minimal erythrocyte lysis indicates that the nanoparticles preserve the integrity of red blood cell membranes under physiological conditions. The observed low hemolytic potential suggests that the nanocomposite is suitable for biomedical applications involving direct blood contact. These findings are consistent with the previous studies indicating that surface-functionalized metal oxide nanoparticles often display enhanced blood compatibility due to reduced surface reactivity and improved colloidal stability [2, 3]. These results highlight the potential of ZnO/PDA nanocomposite for integration into hemocompatible therapeutic and diagnostic platforms (Fig. 5).

## Antibacterial activity of ZnO/PDA nanocomposite

The antibacterial efficacy of the ZnO/PDA nanocomposite was evaluated against *Bacillus cereus* (Gram-positive) and *E. coli* (Gram-negative) using the agar-well

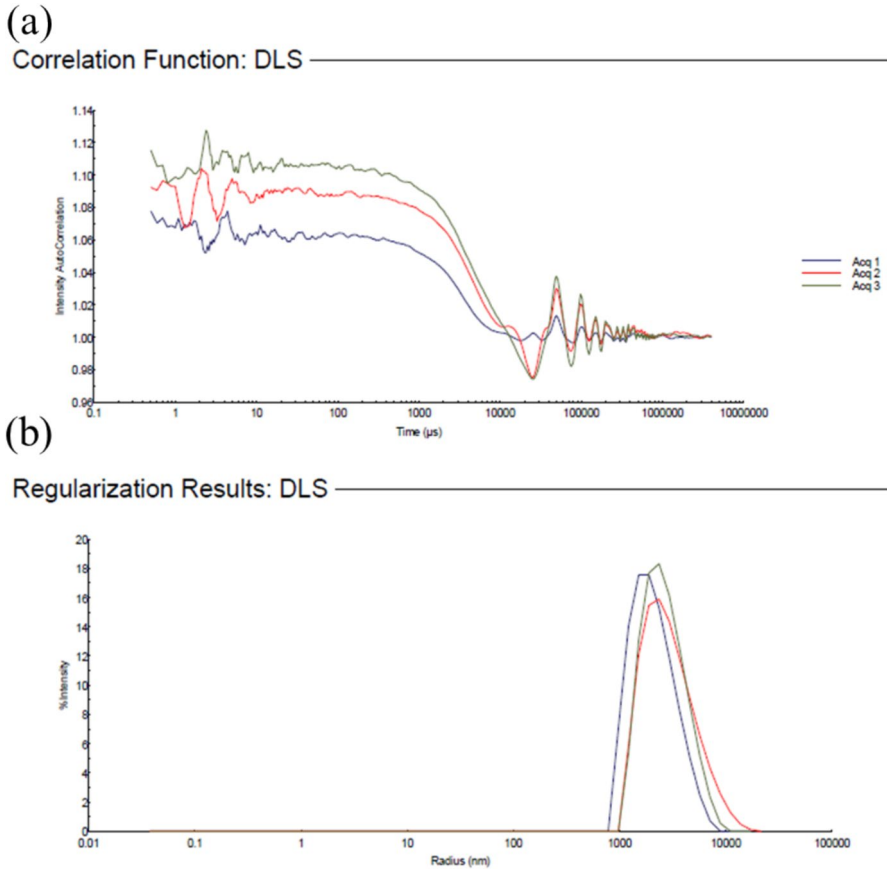


**Fig. 4** Dynamic light scattering (DLS) analysis of ZnO/PDA nanocomposite dispersed in distilled water: **a** Correction function decay profile and **b** DLS regularization profile

diffusion method, as depicted in Fig. 6. The nanocomposite exhibited notable zones of inhibition (ZOI) of 11.56 mm for *B. cereus* (Fig. 6c) and 11.80 mm for *E. coli* (Fig. 6f), highlighting its broad-spectrum antimicrobial potential. These results are consistent with the previous studies, notably paralleling the antibacterial performance of ZnO/antibiotic combinations reported by Chaudhari et al. [78] and the standalone ZnO activity described by Meruvu et al. [79]. Control experiments using unmodified ZnO, Fig. 6b and e confirmed its concentration-dependent antimicrobial action, with negligible inhibition observed at low concentrations, where the ZOI was effectively absent. This trend aligns with findings by Jin and Jin [80], who demonstrated that ZnO alone requires substantially higher concentrations to achieve comparable antimicrobial outcomes. The enhanced antimicrobial activity of the ZnO/PDA nanocomposite is attributed to a synergistic interplay between the oxidative stress-inducing properties of ZnO and the multifaceted biological activity of PDA. ZnO is known to produce bactericidal reactive

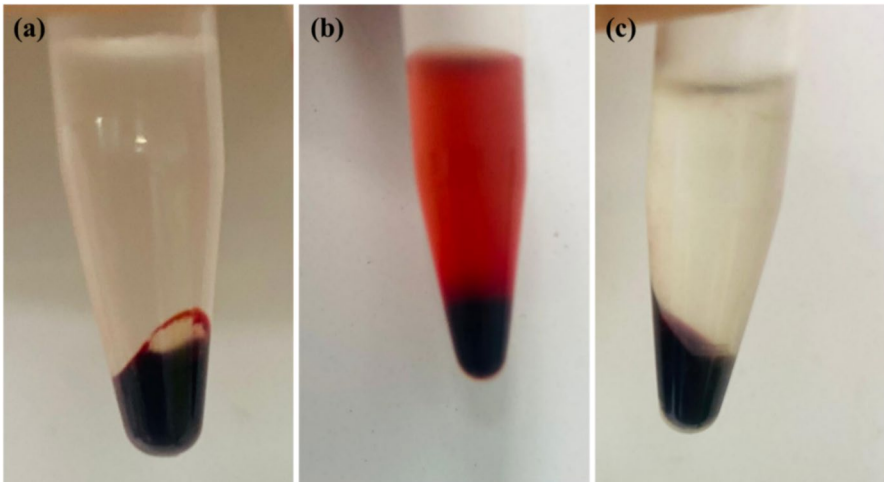


**Fig. 5** Hemolysis assay evaluating the blood compatibility of ZnO/PDA nanocomposite: **a** saline-treated erythrocytes as a negative control (non-hemolytic), **b** distilled water-treated erythrocytes as a positive control (complete hemolysis), and **c** ZnO/PDA-treated erythrocytes demonstrating hemocompatibility

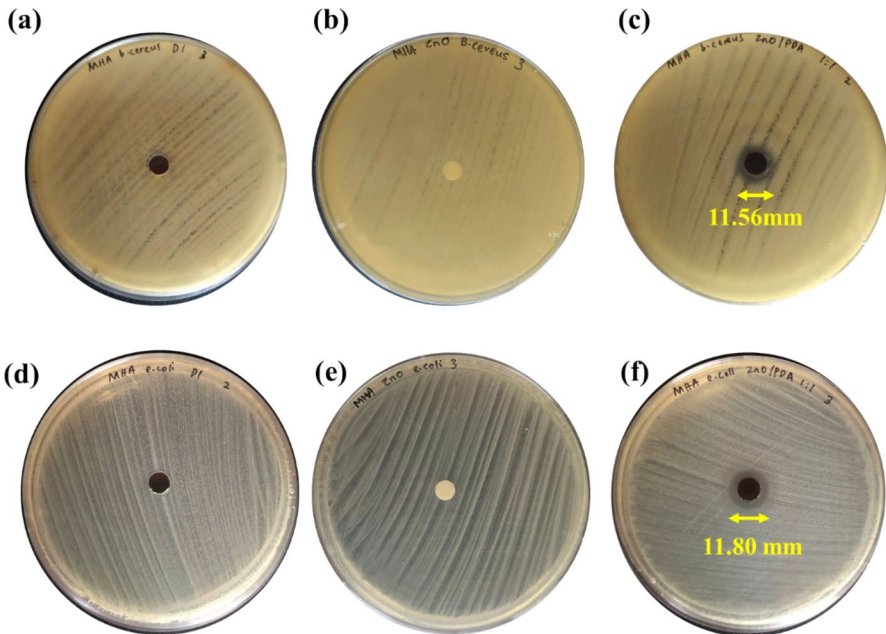


**Fig. 6** Antibacterial activity assessment through zone of inhibition (ZOI) assays: (Top row) *B. cereus* (Gram-positive) treated with **a** negative control (DI water), **b** pure ZnO NPs, and **c** ZnO/PDA nanocomposite. (Bottom row) *E. coli* (Gram-negative) treated with **d** negative control (DI water), **e** pure ZnO, and **f** ZnO/PDA

oxygen species, including hydrogen peroxide, particularly when coordinated with a catechol group [81–85]. The PDA layer likely intensifies this effect by enhancing bacterial surface adhesion through its catechol-rich interface [86], concentrating oxidative damage at the cell envelope. Moreover, PDA itself contributes to antimicrobial action by disrupting essential bacterial proteins through surface entrapment, potentially inducing apoptosis-like cell death, a phenomenon supported by our molecular docking results (Figs. 8 and 9) and corroborated by prior literature [48]. Although not directly quantified here, the redox-active nature of PDA is also expected to promote additional ROS generation via electron transfer processes [87], thereby amplifying the overall bactericidal effect. Together, these synergistic interactions explain the superior antimicrobial performance of ZnO/PDA nanocomposites compared to unmodified ZnO and underscore their potential as multifunctional antibacterial platforms.

The antibacterial potency of the ZnO/PDA nanocomposite was further quantified by determining its minimum inhibitory concentration (MIC) and minimum bactericidal concentration (MBC) against *E. coli* and *B. cereus*. MIC values were assessed by monitoring turbidity and confirmed through optical density measurements at 600 nm ( $OD_{600}$ ). The MIC values were found to be 3.12 mg/L for *E. coli* and 6.25 mg/L for *B. cereus*, indicating a higher sensitivity of the Gram-negative strain to the composite system. Subsequently, the MBC was established by visually inspecting bacterial growth inhibition and correlating it with turbidity data (Fig. 7). The MBC was determined to be 25 mg/L for both bacterial strains. The comparatively low MIC values, combined with the higher MBC threshold, suggest a primarily bacteriostatic mode of action at lower concentrations, with bactericidal activity manifesting at elevated levels. These findings reinforce the composite's potential as an effective antimicrobial agent with broad-spectrum capabilities at low dosages.

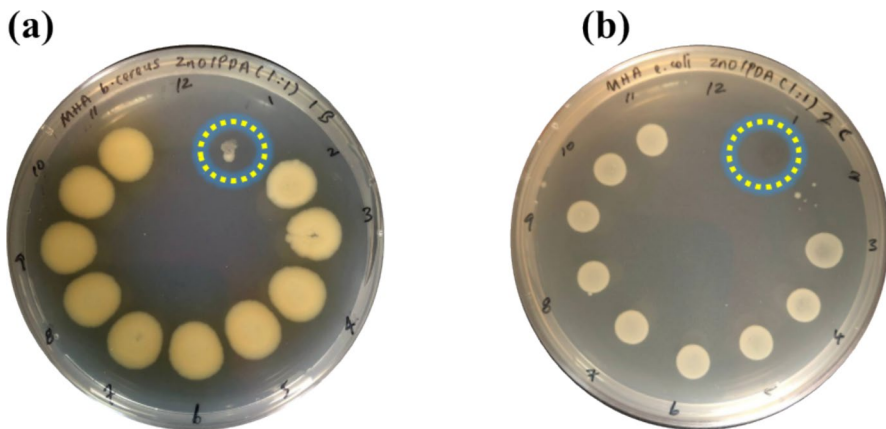


**Fig. 7** Minimum bactericidal concentration for ZnO/PDA against **a** *B. cereus* and **b** *E. coli*

## Molecular docking analysis

In silico approaches offer a powerful means to elucidate the molecular mechanisms by which chemical agents interact with macromolecules and ligands. These computational techniques enable the prediction of potential molecular pathways and provide insights that can guide and complement in vitro analysis. Despite their utility, molecular docking operates under idealized and static conditions, in contrast with the dynamic and often transient nature of molecular interactions in vivo. Consequently, while docking reveals probable binding poses and affinity energies, it does not always capture the full complexity of a chemical's mechanism of action [88]. To explore the interaction potential of the synthesized ZnO/PDA nanocomposite, molecular docking studies were conducted against dihydroorotase enzymes derived from *Bacillus cereus* and *E. coli*. The CB-Dock platform was employed for this analysis, a blind docking tool specifically tailored for protein–ligand interactions. CB-Dock integrates a cavity detection algorithm (CurPocket) that autonomously identifies potential binding sites based on surface curvature. It then calculates the geometric center and dimensions of these binding cavities to configure docking boxes that fit the ligand optimally. Subsequent docking simulations were executed using AutoDock Vina, a widely validated engine for pose prediction and binding energy estimation. The CB-Dock workflow not only enhances the hit rate but also improves docking accuracy by restricting pose sampling to biologically relevant cavities. In this study, the grid parameters were adaptively set for each ligand–protein pair to maximize docking performance. The resulting binding affinities and optimal poses provide preliminary mechanistic insights into how the ZnO/PDA nanocomposite may interfere with bacterial enzyme activity at the molecular level [60, 88].

### Docking interaction with *Bacillus cereus* (PDB ID: 3B55)

To evaluate the potential antibacterial mechanism of the ZnO/PDA nanocomposite, molecular docking studies were performed against the dihydroorotase enzyme from *Bacillus cereus* (Q81BN2\_BACCR) protein, with Clindamycin employed as a reference control. The results, summarized in Table 3, highlight the distinct binding interactions of both ligands within the active site cavity. Clindamycin exhibited a binding free energy of  $-6.5$  kcal/mol. It formed four conventional hydrogen bonds with residues His85, Glu113, Asp172, Tyr320, and Gly407. Additionally, hydrophobic contacts were observed with His85, Ile408, Ile319, Tyr280, and His283. Notably, the drug also engaged in two ionic interactions involving His85 and His283, along with a  $\pi$ – $\pi$  stacking interaction with His85 (Fig. 8B), confirming its favorable yet moderate binding profile. In contrast, the synthesized ZnO/PDA nanocomposite demonstrated a significantly enhanced binding affinity, with a calculated binding energy of  $-10.3$  kcal/mol. It is formed three hydrogen bonds involving key residues such as Asp172, Ile173, Gln174, Asp212, Tyr320, Phe279, Thr271, His309, and Glu113. A broader spectrum of hydrophobic interactions was also detected, notably with Gln264, Ile173, Phe265, Thr267, Leu269, Phe279, Thr278, Tyr280, Ile314,

**Table 3** Molecular docking results of ZnO-dopamine with *Bacillus cereus* and *E. coli* dihydroorotase

Compound Name	Vina Score	Cavity Size	Bound Amino Acids
<i>Bacillus cereus</i> (PDB ID: 3B55)			
ZnO/PDA	- 10.3	2391	Asp172, Ile173, Gln174, Asp212, Tyr320, Phe279, Thr271, His309, Glu113 (H-B), Gln264, Ile173, Phe265, Thr267, Leu269, Phe279, Thr278, Tyr280, Ile314, Phe318 (C-H), His85, His283 (ionic), Tyr280 (pi-pi stacking)
Clindamycin	- 6.5	2391	His85, Glu113, Asp172, Tyr320, Gly407 (H-B), His85, Ile408, Ile319, Tyr280, His283 (C-H), His85, His283 (ionic), His85 (pi-pi stacking)
<i>E. coli</i> dihydroorotase (PDB ID: 2EG7)			
ZnO/PDA	- 8.4	636	Asn94, Phe93, Phe98, Gly96, Thr99, Tyr303, Gly133 (H-B), Glu95, Phe93, Arg59, Leu303 (C-H)
Clindamycin	- 6.4	636	Gly133, Thr99, Phe98, Gly96, Met96, Pro74, Thr73, Pro306 (H-B), Phe93, Leu305, Thr99, Leu75, Arg59(C-H)

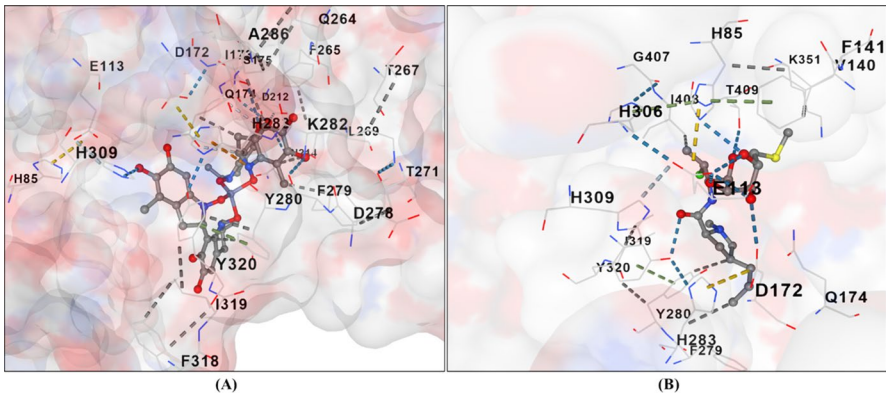


**Fig. 8** Molecular docking of Q81BN2\_BACCR protein from *Bacillus cereus* (PDB ID: 3B55) with a ZnO-dopamine and **b** reference drug Clindamycin

and Phe318. Two ionic interactions were identified with His85 and His283, mirroring those seen with Clindamycin. Furthermore, a strong  $\pi$ - $\pi$  stacking interaction was observed with Tyr280 (Fig. 8A).

The superior binding energy of ZnO/PDA compared to the reference drug suggests a more stable and favorable interaction with the bacterial target. This enhanced affinity is likely attributable to the multifunctional surface of polydopamine, which provides diverse binding modes including hydrogen bonding,  $\pi$ - $\pi$  stacking, and ionic interactions. These findings suggest that the ZnO/PDA composite could serve as a potent antibacterial agent, potentially outperforming conventional antibiotics through a multifaceted binding mechanism.

### Docking interaction with the *E. coli* dihydroorotase (PDB ID: 2EG7)

To further explore the antibacterial potential of the synthesized ZnO/PDA nanocomposite, molecular docking was conducted against *E. coli* dihydroorotase (PDB ID: 2EG7) (Table 3), a critical enzyme involved in the pyrimidine biosynthesis pathway. Clindamycin, a clinically established antibiotic, served as the reference compound in this analysis. Clindamycin exhibited a binding energy of  $-6.4$  kcal/mol, forming eight hydrogen bonds with key residues including Gly133, Thr99, Phe98, Gly96, Met96, Pro74, Thr73, and Pro306. In addition, five hydrophobic interactions were observed with Phe93, Leu305, Thr99, Leu75, and Arg59, collectively stabilizing the drug within the enzyme's active site (Fig. 9b). In contrast, the ZnO/PDA nanocomposite displayed a significantly improved binding profile, with a minimum binding energy of  $-8.4$  kcal/mol, surpassing both Clindamycin and the standard comparator drug, novobiocin (Table 3). The compound formed seven hydrogen bonds involving Asn94, Phe93, Phe98, Gly96, Thr99, Tyr303, and Gly133. Furthermore, it engaged in five hydrophobic interactions with residues Phe93, Leu305, Thr99, Leu75, and Arg59, consistent with the interaction pattern seen in the Clindamycin complex (Fig. 9a).

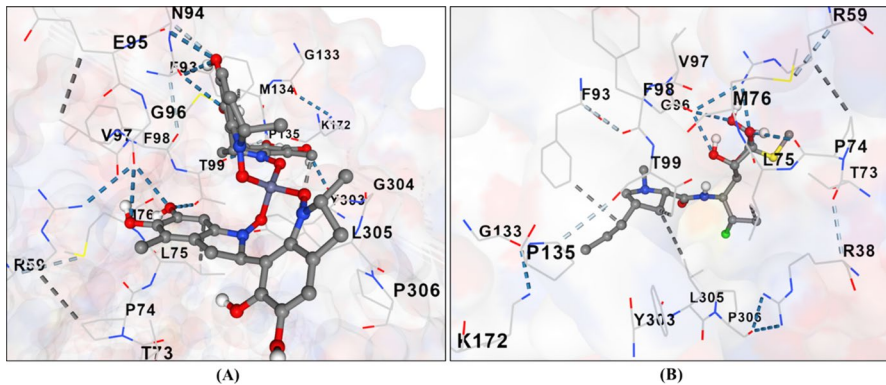


**Fig. 9** Molecular docking of *E. coli* dihydroorotase (PDB ID: 2EG7) with **a** ZnO-dopamine and **b** reference drug Clindamycin

## Conclusion

In this study, we successfully synthesized ZnO/polydopamine (ZnO/PDA) nanocomposites through a facile one-step self-polymerization strategy, resulting in well-defined spherical particles with an average diameter of  $\sim 200$  nm. Comprehensive physicochemical characterization, including UV–Vis spectroscopy, X-ray diffraction (XRD), Fourier-transform infrared spectroscopy (FT-IR), field emission scanning electron microscopy (FESEM), and energy-dispersive X-ray spectroscopy (EDS), confirmed the preservation of the ZnO wurtzite crystal structure and verified effective PDA surface functionalization. The observed popcorn-like morphology, coupled with the retention of key structural features, highlights the successful integration of PDA without compromising the inherent crystallinity of ZnO. The ZnO/PDA nanocomposites demonstrated potent antibacterial activity against both *Bacillus cereus* (Gram-positive) and *E. coli* (Gram-negative), as evidenced by inhibition zone assays and minimum inhibitory/bactericidal concentration measurements. Notably, *in silico* molecular docking studies revealed that ZnO/PDA exhibited stronger binding affinities ( $-10.3$  kcal/mol and  $-8.4$  kcal/mol, respectively) to bacterial dihydroorotase enzymes than the reference antibiotic clindamycin, suggesting potential for broad-spectrum antimicrobial activity via multiple mechanistic pathways. These findings contribute to Sustainable Development Goal 3 (Good Health and Well-being) by offering an alternative approach to combat antibiotic-resistant pathogens and align with SDG 9 (Industry, Innovation, and Infrastructure) by leveraging a low-energy, scalable synthesis for advanced nanomaterials. Nonetheless, key limitations remain. The precise antibacterial mechanisms, such as reactive oxygen species (ROS) generation, membrane disruption, or intracellular targeting, have not been experimentally elucidated. Furthermore, while molecular docking offers predictive insight, cellular uptake, cytotoxicity, and *in vivo* efficacy remain unverified. Long-term stability and biocompatibility assessments are critical before clinical translation. Overall, this work positions ZnO/PDA nanocomposites as a promising platform for next-generation antimicrobial coatings, particularly for medical devices and contact

surfaces. Future studies should integrate mechanistic assays, cytotoxicity profiling, and in vivo testing to fully realize their therapeutic and translational potential.

**Acknowledgements** The authors would like to thank the Ministry of Higher Education Malaysia under The Fundamental Research Grant Scheme No. FRGS/1/2021/TKO/UMP/02/75 (RDU210141) for the research financial support.

**Author contribution** A. Yasin Albarqouni; B. Miah Roney; C. Kwak Fenf Chong; D. Mohammad. R. Thalji; E. Gholamhassan najafi; F. Arman Abdullah. A: Conceptualization, Wrote original manuscript draft, Data analysis, and Wrote revised draft. B: Molecular Docking analysis C: Revise manuscript D: Revise manuscript and Data curing E: Revise the manuscript F: Conceptualization, Revise the manuscript, Supervision, Write revised manuscript draft, Funding.

**Funding** Open access funding provided by The Ministry of Higher Education Malaysia and Universiti Malaysia Pahang Al-Sultan Abdullah.

**Data availability** No datasets were generated or analysed during the current study.

## Declarations

**Conflict of interest** The authors have no relevant financial or non-financial interests to disclose.

**Open Access** This article is licensed under a Creative Commons Attribution-NonCommercial-NoDerivatives 4.0 International License, which permits any non-commercial use, sharing, distribution and reproduction in any medium or format, as long as you give appropriate credit to the original author(s) and the source, provide a link to the Creative Commons licence, and indicate if you modified the licensed material. You do not have permission under this licence to share adapted material derived from this article or parts of it. The images or other third party material in this article are included in the article's Creative Commons licence, unless indicated otherwise in a credit line to the material. If material is not included in the article's Creative Commons licence and your intended use is not permitted by statutory regulation or exceeds the permitted use, you will need to obtain permission directly from the copyright holder. To view a copy of this licence, visit <http://creativecommons.org/licenses/by-nc-nd/4.0/>.

## References

1. Noori AF, Moustafa NM, Hamid KL (2020) Microbial corrosion study using Tafel principles of polarization. IOP Conf Ser Mater Sci Eng. <https://doi.org/10.1088/1757-899X/745/1/012067>
2. Hamid LL, Hassan MH, Obaid AS (2024) Construction of Sodium alginate/palladium nanoparticles SA/Pd NPs aerogel for in vitro and in vivo antibacterial and wound healing applications. J Clust Sci 35:2069–2080. <https://doi.org/10.1007/s10876-024-02643-8>
3. Hamid LL, Hassan MH, Obaid AS (2024) Chitosan aerogel loaded with biogenic palladium nanoparticles CH/Pd NPs exert antibacterial activity and wound addressing application in vitro and in vivo against bacterial skin infections. J Mol Struct 1315:138983. <https://doi.org/10.1016/j.molstruc.2024.138983>
4. Hamid LL, Hamed H, Al-Fahdawi AM et al (2024) Truffle mediated preparation of bacterial culture medium and mycosynthesis of titanium oxide nanoparticles loaded with polyvinyl alcohol/sodium alginate aerogel beads for antibacterial activity. J Sol-Gel Sci Technol 112:512–523. <https://doi.org/10.1007/s10971-024-06541-3>
5. Carlin F, Fricker M, Pielaat A et al (2006) Emetic toxin-producing strains of *Bacillus cereus* show distinct characteristics within the *Bacillus cereus* group. Int J Food Microbiol 109:132–138. <https://doi.org/10.1016/j.ijfoodmicro.2006.01.022>
6. Rahnama H, Azari R, Yousefi MH et al (2023) A systematic review and meta-analysis of the prevalence of *Bacillus cereus* in foods. Food Control 143:109250

7. Jia Q, Song Q, Li P, Huang W (2019) Rejuvenated photodynamic therapy for bacterial infections. *Adv Healthc Mater* 8:1900608
8. Merker M, Tueffers L, Vallier M et al (2020) Evolutionary approaches to combat antibiotic resistance: opportunities and challenges for precision medicine. *Front Immunol* 11:1938
9. Mujaddidi N, Nisa S, Al Ayoubi S et al (2021) Pharmacological properties of biogenically synthesized silver nanoparticles using endophyte *Bacillus cereus* extract of Berberis lyceum against oxidative stress and pathogenic multidrug-resistant bacteria. *Saudi J Biol Sci* 28:6432–6440. <https://doi.org/10.1016/j.sjbs.2021.07.009>
10. Zhao X, Tang H, Jiang X (2022) Deploying gold nanomaterials in combating multi-drug-resistant bacteria. *ACS Nano* 16:10066–10087
11. Abebe B, Zereffa EA, Tadesse A, Murthy HCA (2020) A review on enhancing the antibacterial activity of ZnO: mechanisms and microscopic investigation. *Nanoscale Res Lett* 15:1–19
12. Zhang C, Li X, Zhang Z et al (2024) Morphological effect of ZIFs as the promotion of surface-potential-adsorption for antibacterial performance. *J Inorg Organomet Polym Mater*. <https://doi.org/10.1007/s10904-023-02971-8>
13. Zhang Q, Qiao Q, Wang Z et al (2023) Covalent bonding enhanced polypropylene based T-ZIF-8 masterbatch with superior photocatalytic and antibacterial performances. *J Inorg Organomet Polym Mater* 33:1219–1233. <https://doi.org/10.1007/s10904-023-02576-1>
14. Abd-Elnaiem AM, Rashad M, Hanafy TA, Shaalan NM (2023) Improvement of optical properties of functionalized polyvinyl alcohol-zinc oxide hybrid nanocomposites for wide UV optoelectronic applications. *J Inorg Organomet Polym Mater* 33:2429–2444. <https://doi.org/10.1007/s10904-023-02616-w>
15. Acikbas G, Hindi H (2024) The effect of a composite hydrophobic coating with zinc oxide on the characteristics of polyester matrix composite surfaces. *J Inorg Organomet Polym Mater* 34(1):419–429. <https://doi.org/10.1007/s10904-023-02842-2>
16. Summer M, Ali S, Tahir HM et al (2024) Mode of action of biogenic silver, zinc, copper, titanium and cobalt nanoparticles against antibiotics resistant pathogens. *J Inorg Organomet Polym Mater* 34(4):1417–1451
17. Kalakonda P, Mandal P, Laxmi Mynepally S et al (2024) Comparison of multi-metallic nanoparticles-alternative antibacterial agent: understanding the role of their antibacterial properties. *J Inorg Organomet Polym Mater* 34:2203–2218. <https://doi.org/10.1007/s10904-023-02960-x>
18. Idris DS, Roy A, Subramanian A et al (2024) Bio-fabrication of silver-zinc bimetallic nanoparticles and its antibacterial and dye degradation activity. *J Inorg Organomet Polym Mater* 34:1908–1919. <https://doi.org/10.1007/s10904-023-02936-x>
19. Alturki AM (2022) Facile synthesis route for chitosan nanoparticles doped with various concentrations of the biosynthesized copper oxide nanoparticles: electrical conductivity and antibacterial properties. *J Mol Struct*. <https://doi.org/10.1016/j.molstruc.2022.133108>
20. Farfán RA, Britos ML, Gómez MI et al (2022) Crystal and spectroscopic structure and biological activity of a new lapacholate complex with zinc(II), a potential antibacterial. *J Mol Struct* 1258:132654
21. Sharma N, Aggarwal N, Kumari S et al (2024) Exploring physicochemical characteristics and antimicrobial efficacy of biosynthesized zinc oxide nanoparticles using *Lantana camara* leaf extract. *J Mol Struct*. <https://doi.org/10.1016/j.molstruc.2023.137396>
22. Mbatu PS, Toh-Boyo GM, Ghogomu JN et al (2024) Spectroscopic, density functional theory and molecular docking studies of zinc (II) and nickel (II) complexes of N<sup>1</sup>-(furan-2-ylmethylene) furan-2-carbohydrazide as potential antibacterial drug. *J Mol Struct*. <https://doi.org/10.1016/j.molstruc.2024.137716>
23. Mohamad Sukri SNA, Shameli K, Mei-Theng Wong M et al (2019) Cytotoxicity and antibacterial activities of plant-mediated synthesized zinc oxide (ZnO) nanoparticles using *Punica*

- granatum (pomegranate) fruit peels extract. *J Mol Struct* 1189:57–65. <https://doi.org/10.1016/j.molstruc.2019.04.026>
24. Pillai AM, Sivasankarapillai VS, Rahdar A et al (2020) Green synthesis and characterization of zinc oxide nanoparticles with antibacterial and antifungal activity. *J Mol Struct*. <https://doi.org/10.1016/j.molstruc.2020.128107>
  25. Dappula SS, Kandrakonda YR, Shaik JB et al (2023) Biosynthesis of zinc oxide nanoparticles using aqueous extract of *Andrographis alata*: characterization, optimization and assessment of their antibacterial, antioxidant, antidiabetic and anti-Alzheimer's properties. *J Mol Struct*. <https://doi.org/10.1016/j.molstruc.2022.134264>
  26. Omran BA, Baek KH (2024) Dual extracellular mycofabrication of cobalt and zinc nano metal oxides mediated by mycelial-cell free filtrate of *Aspergillus sojae*: characterization and assessment of antibacterial activity. *J Mol Struct*. <https://doi.org/10.1016/j.molstruc.2023.137190>
  27. Abdulrahman MF, Al-Rawi AS, Hamid LL et al (2024) Preparation of polyvinyl alcohol (PVA) aerogel microsphere loaded with biogenic zinc oxide nanoparticles as potential antibacterial drug. *J Mol Struct*. <https://doi.org/10.1016/j.molstruc.2024.137901>
  28. Dayu X, Mingxing L, Ansari KR, Singh A (2022) Synthesis of novel nano polymeric composite of zinc oxide and its application in corrosion inhibition of tubular steel in sweet corrosive medium. *J Mol Liq* 359:119327. <https://doi.org/10.1016/j.molliq.2022.119327>
  29. Elzeref AS, Elgammal WE, Mosaad A et al (2023) Thione tautomer of hydrazone-carbodithioate chelator-derived Cu (II) and Zn (II) complexes as potential antibacterial agents : DFT computations and UV-assisted photocatalytic degradation of Rose Bengal dye. *J Mol Liq* 385:122325. <https://doi.org/10.1016/j.molliq.2023.122325>
  30. Thangapandi JR, Chelliah P, Balakrishnan S et al (2021) Antibacterial and photocatalytic aspects of zinc oxide nanorods synthesized using *Piper nigrum* seed extract. *J Nanostructure Chem* 11:549–560. <https://doi.org/10.1007/s40097-020-00383-5>
  31. Thunugunta T, Reddy AC, Seetharamaiah SK et al (2018) Impact of Zinc oxide nanoparticles on eggplant (*S. melongena*): studies on growth and the accumulation of nanoparticles. *IET Nanobiotechnol* 12:706–713. <https://doi.org/10.1049/iet-nbt.2017.0237>
  32. Sharma RK, Ghose R (2015) Synthesis of zinc oxide nanoparticles by homogeneous precipitation method and its application in antifungal activity against *Candida albicans*. *Ceram Int* 41:967–975. <https://doi.org/10.1016/j.ceramint.2014.09.016>
  33. Sirelkhatim A, Mahmud S, Seeni A et al (2015) Review on zinc oxide nanoparticles: antibacterial activity and toxicity mechanism. *Nano-Micro Lett* 7:219–242
  34. Wang L, Wang Z, Wang Z et al (2021) Enhancement of antibacterial function by incorporation of silver-doped ZnO nanocrystals onto a laser-induced graphene surface. *RSC Adv* 11:33883–33889. <https://doi.org/10.1039/d1ra06390a>
  35. Nagar V, Singh T, Tiwari Y et al (2022) ZnO nanoparticles: exposure, toxicity mechanism and assessment. *Mater Today Proc* 69:56–63. <https://doi.org/10.1016/j.matpr.2022.09.001>
  36. Ma H, Williams PL, Diamond SA (2013) Ecotoxicity of manufactured ZnO nanoparticles—a review. *Environ Pollut* 172:76–85
  37. Singh J, Dutta T, Kim KH et al (2018) “Green” synthesis of metals and their oxide nanoparticles: applications for environmental remediation. *J Nanobiotechnol*. <https://doi.org/10.1186/s12951-018-0408-4>
  38. Zarghami S, Mohammadi T, Sadrzadeh M, Van der Bruggen B (2020) Bio-inspired anchoring of amino-functionalized multi-wall carbon nanotubes (N-MWCNTs) onto PES membrane using polydopamine for oily wastewater treatment. *Sci Total Environ*. <https://doi.org/10.1016/j.scitotenv.2019.134951>

39. Xu X, Sun L, Bai B et al (2019) Interfacial assembly of mussel-inspired polydopamine@Ag core-shell nanoparticles as highly recyclable catalyst for nitroaromatic pesticides degradation. *Sci Total Environ* 665:133–141. <https://doi.org/10.1016/j.scitotenv.2019.02.105>
40. Wan Y, Liu X, Liu P et al (2018) Optimization adsorption of norfloxacin onto polydopamine microspheres from aqueous solution: kinetic, equilibrium and adsorption mechanism studies. *Sci Total Environ* 639:428–437. <https://doi.org/10.1016/j.scitotenv.2018.05.171>
41. Zhang Y, Huang S, Mei B et al (2023) Mussel inspired synthesis of polydopamine/polyethyleneimine-grafted fly ash composite adsorbent for the effective separation of U(VI). *Sci Total Environ*. <https://doi.org/10.1016/j.scitotenv.2023.162841>
42. Bhogal S, Mohiuddin I, Kumar S et al (2022) Self-polymerized polydopamine-imprinted layer-coated carbon dots as a fluorescent sensor for selective and sensitive detection of 17 $\beta$ -oestradiol. *Sci Total Environ*. <https://doi.org/10.1016/j.scitotenv.2022.157356>
43. Wu Y, Niu J, Yuan X et al (2023) Polydopamine and calcium functionalized fiber carrier for enhancing microbial attachment and Cr(VI) resistance. *Sci Total Environ*. <https://doi.org/10.1016/j.scitotenv.2023.166626>
44. Cheng S, Pan X, Zhang C et al (2022) UV-assisted ultrafast construction of robust Fe<sub>3</sub>O<sub>4</sub>/polydopamine/Ag fenton-like catalysts for highly efficient micropollutant decomposition. *Sci Total Environ*. <https://doi.org/10.1016/j.scitotenv.2021.151182>
45. Khodakarami M, Honaker R (2024) Photothermal self-floating aerogels based on chitosan functionalized with polydopamine and carbon nanotubes for removal of arsenic from wastewater. *Sci Total Environ*. <https://doi.org/10.1016/j.scitotenv.2023.169519>
46. Albarqouni Y, Banius E, Bakar NHA, Abdullah A (2023) Uncovering intelligent self-healing coating: Synthesis strategies, performance, and evaluation techniques—a review. *Int J Corros Scale Inhib* 12:1592–1609
47. Wang Y, Qi W, Mao Z et al (2023) rPDAs doped antibacterial MOF-hydrogel: bio-inspired synergistic whole-process wound healing. *Mater Today Nano*. <https://doi.org/10.1016/j.mtnano.2023.100363>
48. Adnan NNM, Sadrearhami Z, Bagheri A et al (2018) Exploiting the versatility of Polydopamine-coated nanoparticles to deliver nitric oxide and combat bacterial biofilm. *Macromol Rapid Commun*. <https://doi.org/10.1002/marc.201800159>
49. Liu Y, Ai K, Lu L (2014) Polydopamine and its derivative materials: synthesis and promising applications in energy, environmental, and biomedical fields. *Chem Rev* 114:5057–5115
50. Benhebal H, Chaib M, Salmon T et al (2013) Photocatalytic degradation of phenol and benzoic acid using zinc oxide powders prepared by the sol-gel process. *Alexandria Eng J* 52(3):517–523. <https://doi.org/10.1016/j.aej.2013.04.005>
51. Qiao Y, Jia X, Wang Y et al (2024) Polydopamine-encapsulated zinc peroxide nanoparticles to target the metabolism-redox circuit against tumor adaptability for mild photothermal therapy. *Nanoscale Horiz* 9:1002–1012. <https://doi.org/10.1039/d4nh00070f>
52. García-Mayorga JC, Rosu HC, Jasso-Salcedo AB, Escobar-Barrios VA (2023) Kinetic study of polydopamine sphere synthesis using TRIS: relationship between synthesis conditions and final properties. *RSC Adv*. <https://doi.org/10.1039/d2ra06669f>
53. Albarqouni Y, Ali GAM, Lee SP et al (2021) Dual-functional single stranded deoxyribonucleic acid for graphene oxide reduction and charge storage enhancement. *Electrochim Acta* 399:139366. <https://doi.org/10.1016/j.electacta.2021.139366>
54. Albarqouni YMY, Lee SP, Ali GAM et al (2022) Facile synthesis of reduced graphene oxide aerogel in soft drink as supercapacitor electrode. *J Nanostructure Chem* 12:417–427. <https://doi.org/10.1007/s40097-021-00424-7>
55. ASTM (2020) Standard practice for assessment of hemolytic properties of materials - F 756–00. In: American society for testing and materials. pp 1–5
56. Hamid LL, Al-Meani SAL (2021) Extraction and purification of a lectins from Iraqi Truffle (*Terfezia* sp.). *Egypt J Chem* 64:2983–2987. <https://doi.org/10.21608/ejchem.2021.56025.3201>

57. Hossain ML, Lim LY, Hammer K et al (2022) A review of commonly used methodologies for assessing the antibacterial activity of honey and honey products. *Antibiotics* 11:975
58. Serrano Cardona L, Muñoz Mata E (2013) Paraninfo digital
59. Kowalska-Krochmal B, Dudek-Wicher R (2021) The minimum inhibitory concentration of antibiotics: methods, interpretation, clinical relevance. *Pathogens* 10:1–21
60. Roney M, Issahaku AR, Forid MS et al (2023) In silico evaluation of usnic acid derivatives to discover potential antibacterial drugs against DNA gyrase B and DNA topoisomerase IV. *J Biomol Struct Dyn* 41:14904–14913. <https://doi.org/10.1080/07391102.2023.2193996>
61. Enosi Tuipulotu D, Mathur A, Ngo C, Man SM (2021) *Bacillus cereus*: epidemiology, virulence factors, and host-pathogen interactions. *Trends Microbiol* 29:458–471
62. Huang CY (2025) The loop-in binding mode of dihydroorotase: implications for ligand binding and therapeutic targeting. *Int J Mol Sci* 26:1359. <https://doi.org/10.3390/ijms26031359>
63. Liu Y, Grimm M, Dai WT et al (2020) CB-Dock: a web server for cavity detection-guided protein–ligand blind docking. *Acta Pharmacol Sin* 41:138–144. <https://doi.org/10.1038/s41401-019-0228-6>
64. Senthilkumar N, Nandhakumar E, Priya P et al (2017) Synthesis of ZnO nanoparticles using leaf extract of: *Tectona grandis* (L.) and their anti-bacterial, anti-arthritic, anti-oxidant and in vitro cytotoxicity activities. *New J Chem* 41:10347–10356. <https://doi.org/10.1039/c7nj02664a>
65. Ristić M, Musić S, Ivanda M, Popović S (2005) Sol-gel synthesis and characterization of nanocrystalline ZnO powders. *J Alloys Compd* 397:1–4
66. Kolodziejczak-Radzimska A, Jesionowski T (2014) Zinc oxide-from synthesis to application: a review. *Materials (Basel)* 7:2833–2881
67. Thema FT, Manikandan E, Dhlamini MS, Maaza M (2015) Green synthesis of ZnO nanoparticles via *Agathosma betulina* natural extract. *Mater Lett* 161:124–127. <https://doi.org/10.1016/j.matlet.2015.08.052>
68. Zou Y, Chen X, Yang P et al (2020) Regulating the absorption spectrum of polydopamine. *Sci Adv*. <https://doi.org/10.1126/sciadv.abb4696>
69. Qi C, Zhang Y, Tu J (2022) Facile synthesis of  $\epsilon$ -poly-L-lysine-conjugated ZnO@PDA as photo-thermal antibacterial agents for synergistic bacteria killing and biofilm eradication. *Biochem Eng J* 186:108569. <https://doi.org/10.1016/j.bej.2022.108569>
70. Xiong Q, Fang Q, Xu K et al (2021) Near-infrared light-responsive photothermal  $\alpha$ -Fe<sub>2</sub>O<sub>3</sub>@Au/PDA core/shell nanostructure with on-off controllable anti-bacterial effects. *Dalton Trans* 50:14235–14243. <https://doi.org/10.1039/d1dt02251b>
71. Wang HJ, Peng H, Ji WH et al (2024) Photo-responsive polypropylene/zinc oxide/polydopamine-TEMPO composite membranes with light-induced self-sterilization. *Nano Mater Sci*. <https://doi.org/10.1016/j.nanoms.2024.04.012>
72. Tavakoli S, Kharaziha M, Nemati S (2021) Polydopamine coated ZnO rod-shaped nanoparticles with noticeable biocompatibility, hemostatic and antibacterial activity. *Nano-Struct Nano-Objects* 25:100639. <https://doi.org/10.1016/j.nanoso.2020.100639>
73. Elhamdi I, Souissi H, Taktak O et al (2022) Experimental and modeling study of ZnO:Ni nanoparticles for near-infrared light emitting diodes. *RSC Adv* 12:13074–13086. <https://doi.org/10.1039/d2ra00452f>
74. Nie N, He F, Zhang L, Cheng B (2018) Direct Z-scheme PDA-modified ZnO hierarchical microspheres with enhanced photocatalytic CO<sub>2</sub> reduction performance. *Appl Surf Sci* 457:1096–1102. <https://doi.org/10.1016/j.apsusc.2018.07.002>
75. Wilson BK, Prud'homme RK, (2021) Nanoparticle size distribution quantification from transmission electron microscopy (TEM) of ruthenium tetroxide stained polymeric nanoparticles. *J Colloid Interface Sci* 604:208–220. <https://doi.org/10.1016/j.jcis.2021.04.081>
76. Ahmad M, Zhu J (2011) ZnO based advanced functional nanostructures: synthesis, properties and applications. *J Mater Chem* 21:599–614. <https://doi.org/10.1039/c0jm01645d>
77. Wang MH, Ma XY, Zhou F (2015) Synthesis and characterization of monodispersed spherical ZnO nanocrystals in an aqueous solution. *Mater Lett* 142:64–66. <https://doi.org/10.1016/j.matlet.2014.11.126>
78. Chaudhary A, Kumar N, Kumar R, Salar RK (2019) Antimicrobial activity of zinc oxide nanoparticles synthesized from Aloe vera peel extract. *SN Appl Sci*. <https://doi.org/10.1007/s42452-018-0144-2>
79. Meruvu H, Vangalapati M, Chaitanya Chippada S, Rao Bammidi S (2011) Synthesis and characterization of zinc oxide nanoparticles and its antimicrobial activity against *Bacillus subtilis* and *E. coli*. *Rasayan J Chem* 4:217–222

80. Jin SE, Jin HE (2021) Antimicrobial activity of zinc oxide nano/microparticles and their combinations against pathogenic microorganisms for biomedical applications: from physicochemical characteristics to pharmacological aspects. *Nanomaterials* 11:1–35
81. Hwang C, Choi MH, Kim HE et al (2022) Reactive oxygen species-generating hydrogel platform for enhanced antibacterial therapy. *NPG Asia Mater.* <https://doi.org/10.1038/s41427-022-00420-5>
82. Wang Y, Li Z, Hu Y et al (2020) Photothermal conversion-coordinated Fenton-like and photocatalytic reactions of Cu<sub>2</sub>-xSe-Au Janus nanoparticles for tri-combination antitumor therapy. *Biomaterials.* <https://doi.org/10.1016/j.biomaterials.2020.120167>
83. Lakshmi Prasanna V, Vijayaraghavan R (2015) Insight into the mechanism of antibacterial activity of ZnO: surface defects mediated reactive oxygen species even in the dark. *Langmuir* 31:9155–9162. <https://doi.org/10.1021/acs.langmuir.5b02266>
84. Kumar S, Reddy NL, Kushwaha HS et al (2017) Efficient electron transfer across a ZnO–MoS<sub>2</sub>–reduced graphene oxide heterojunction for enhanced sunlight-driven photocatalytic hydrogen evolution. *Chemosuschem* 10:3588–3603. <https://doi.org/10.1002/cssc.201701024>
85. Black KCL, Liu Z, Messersmith PB (2011) Catechol redox induced formation of metal core-polymer shell nanoparticles. *Chem Mater* 23:1130–1135. <https://doi.org/10.1021/cm1024487>
86. Singh I, Dhawan G, Gupta S, Kumar P (2021) Recent advances in a polydopamine-mediated antimicrobial adhesion system. *Front Microbiol* 11:607099
87. Zhang Z, He X, Zhou C et al (2020) Iron magnetic nanoparticle-induced ROS generation from catechol-containing microgel for environmental and biomedical applications. *ACS Appl Mater Interfaces* 12:21210–21220
88. Roney M, Dubey A, Issahaku AR et al (2024) Insights from in silico exploration of major curcumin analogs targeting human dipeptidyl peptidase IV. *J Biomol Struct Dyn.* <https://doi.org/10.1080/07391102.2024.2306197>

**Publisher's Note** Springer Nature remains neutral with regard to jurisdictional claims in published maps and institutional affiliations.

## Authors and Affiliations

Yasin Albarqouni<sup>1,2</sup> · Miah Roney<sup>3,4</sup> · Kwok Feng Chong<sup>3</sup> ·  
 Mohammad R. Thalji<sup>5</sup> · Gholamhassan Najafi<sup>6</sup> · Arman Abdullah<sup>1</sup>

✉ Arman Abdullah  
 armanabdullah@umpsa.edu.my

<sup>1</sup> Faculty of Chemical and Process Engineering Technology, Universiti Malaysia Pahang Al-Sultan Abdullah, Lebuhraya Persiaran Tun Khalil Yaakob, 26300 Kuantan, Pahang, Malaysia

<sup>2</sup> Faculty of Applied Medical Sciences, Clinical Nutrition Department, Al-Azhar University-Gaza, Gaza 1277, Palestine

<sup>3</sup> Faculty of Industrial Sciences and Technology, Universiti Malaysia Pahang Al-Sultan Abdullah, Lebuhraya Persiaran Tun Khalil Yaakob, 26300 Kuantan, Pahang, Malaysia

<sup>4</sup> Centre for Bio-Aromatic Research, Universiti Malaysia Pahang Al-Sultan Abdullah, Lebuhraya Persiaran Tun Khalil Yaakob, 26300 Kuantan, Pahang, Malaysia

<sup>5</sup> Korea Institute of Energy Technology (KENTECH), 21 KENTECH-gil, Naju, Jeollanam-do 58330, Republic of Korea

<sup>6</sup> Centre of Research in Advanced Fluid and Process, Universiti Malaysia Pahang Al-Sultan Abdullah, Lebuhraya Persiaran Tun Khalil Yaakob, 26300 Kuantan, Pahang, Malaysia